



Keywords: anomalous diffraction; diffraction
anomalous fine structure; DAFS.

Diffraction anomalous fine structure: experiment and data analysis

Hubert Renevier^{a*} and Maria Grazia Proietti^b

^aUniversité Grenoble Alpes, CNRS, Grenoble–INP, LMGP, 38016 Grenoble, France, and ^bDepartamento de Física de la Materia Condensada, Universidad de Zaragoza, INMA, CSIC–UNIZAR, Zaragoza, Spain. *Correspondence e-mail: hubert.renevier@grenoble-inp.fr

In this chapter, the main experimental aspects of diffraction anomalous fine-structure spectroscopy (DAFS) are reported. The basic formalism is given in Renevier & Proietti (2022). The most relevant issues concerning data acquisition, data reduction and extended DAFS fitting are highlighted. Multi-wavelength anomalous diffraction is briefly illustrated since it is intimately related to DAFS. A selected bibliography provides several examples of applications that are fundamental for a full understanding of this powerful spectroscopic technique.

1. Introduction

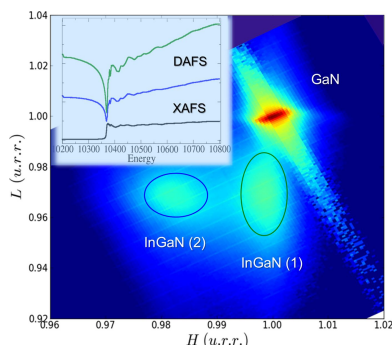
Diffraction anomalous fine-structure spectroscopy (DAFS) provides information about the empty electronic orbitals and the local atomic environment of resonant atoms which are selected by the diffraction condition, thus combining the chemical selectivity of X-ray absorption fine-structure (XAFS) spectroscopy with the space- or site-selectivity of diffraction.

At the turn of the 21st century, increasing interest in structural studies of 0D to 2D epitaxial nanostructures and heterostructures, thin films and nanomaterials more generally led to the development and application of multiwavelength anomalous diffraction (MAD) and DAFS, in combination with XAFS and *ab initio* calculations, to determine strain, atomic composition and atomic long-range and short-range order as well as crystallographic polarity. MAD, DAFS, XAFS and *ab initio* calculations constitute a very efficient and powerful toolset for semiconductor heterostructures and nanostructures (Coraux *et al.*, 2007; Katcho *et al.*, 2011). The reader will find extensive information about DAFS spectroscopy (including DAFS in grazing-incidence geometry) in several review articles (Sorensen *et al.*, 1994; Hodeau *et al.*, 2001; Favre-Nicolin *et al.*, 2012; Renevier & Proietti, 2013).

2. Multiwavelength anomalous diffraction

MAD is commonly used to phase structure factors in molecular crystallography and to determine cation occupancy in long-range ordered crystallographic sites. As shown in Renevier & Proietti (2022), MAD enables mapping of the modulus of the partial structure factors F_A and F_N and the phase difference $\varphi_N - \varphi_A$ from reciprocal-space maps measured at several energies close to the absorption edge of resonant atoms A (N refers to nonresonant atoms).

In the case of homogeneous binary alloys, $\varphi_N - \varphi_A = 0$, where A and N atoms occupy the same crystallographic site, the ratio $|F_A|/|F_N|$ readily gives the A -atom average content in



the isostrain region picked up by the diffraction condition. However, the method applies as long as the isostrain scattering hypothesis is valid, *i.e.* when the heterostructures can be decomposed into isocell lattice-parameter regions which do not interfere, *i.e.* in the presence of large objects and strain gradients (Kegel *et al.*, 2001). In the most general case, the crystallographic structure must be used to refine the occupation factor of the resonant atoms (Renevier *et al.*, 1997).

MAD is an efficient method to disentangle strain and composition. In the following, we mainly focus on energy-scan measurements, data reduction and extended DAFS refinement.

3. Energy-scan diffraction

A DAFS experiment consists of measuring the scattered/diffracted intensity at a fixed point in reciprocal space and $Q = 2\sin\theta/\lambda$ value (where 2θ is the scattering angle) as a function of the X-ray beam energy $E = hc/\lambda$, spanning a typical energy range of 1000 eV across an absorption edge. \mathbf{Q} is the scattering vector, $\mathbf{Q} = \mathbf{k}' - \mathbf{k}$, where \mathbf{k} and \mathbf{k}' are the incoming and outgoing X-ray beam wavevectors, respectively, and E is the X-ray beam energy. A DAFS spectrum cusp, measured over a large energy range (of the order of 1 keV) and a small step size (0.5–5 eV), corresponds to oversampled MAD data which provide very precise values of $|F_A|/|F_N|$ and $\varphi_N - \varphi_A$ (or $|F_A|/|f_A^0|F_T$ and $\varphi_T - \varphi_A$).

If one wants to quantitatively analyze the oscillatory fine structure of the DAFS spectrum, the latter must not present distortions and the monitor-corrected signal-to-noise ratio must be as high as 1000 or greater, *i.e.* comparable requirements to those for obtaining high-quality extended XAFS oscillations. This requires a fixed-exit diffraction beamline with a scanning monochromator coupled to a diffractometer, both with high-precision movements and monochromator dynamical tuning. The stability and footprint of the beam at the sample position are of major importance. To avoid distortions, high precision and reproducibility of the monochromator–diffractometer coupling are essential. For instance, 1 eV resolution at 10 keV with a Si(111) crystal monochromator requires a monochromator angle precision of about 2×10^{-5} rad and therefore the coupling precision must be of the same order (Renevier *et al.*, 2003).

Another source of distortion is multiple Bragg diffraction in the sample or the substrate, which diverts intensity away from the sample. In this case the only way to try to improve the data is to rotate the sample about the azimuthal ψ angle. When using an orientation matrix, its accuracy in tracking the Bragg peak when scanning the energy must be verified. As for XAFS experiments, the incident beam must be carefully monitored, for instance, by measuring the fluorescence signal emitted from a high-purity metal foil of a few micrometres in thickness mounted in vacuum (Renevier *et al.*, 2003).

With regard to detection, 2D pixel detectors have definite advantages in comparison with point or linear detectors. They cope with high counting rates with a low background intensity, allowing the collection of high-quality 3D reciprocal-space

maps close to Bragg peaks on counting timescales of the order of tens of seconds to minutes.

One drawback of 2D detectors is the lack of a sufficient energy resolution to discriminate the fluorescence background. However, most often the 2D detectors are large enough to simultaneously record both the DAFS spectra and the fluorescence background in different regions of interest.

4. Data reduction

In the Born approximation, the intensity of the DAFS spectrum is related to the square modulus of the structure factor according to the formula

$$I(\mathbf{Q}, E) = KD(E)L(\theta, E)A(\theta, E)|F(\mathbf{Q}, E)|^2, \quad (1)$$

where I is corrected for the background intensity (mainly fluorescence yield), K is a scale factor, D is the detector efficiency, L and P are the Lorentz and polarization factors for Thomson scattering, respectively, A is the absorption correction and $F(\mathbf{Q}, E)$ is the structure factor (Als-Nielsen & McMorrow, 2001; Prince, 2006). D takes into account the whole detection setup, comprising the detector efficiency and absorption all the way from the monitor to the diffraction detector. The energy dependence of D is often linear within the energy range of interest (about 1 keV), so that D may be fitted to the DAFS spectrum by a straight line [$D = m(\Delta E + 1)$], where m is the only adjustable parameter, $\Delta E = E - E_0$ and E_0 is the edge energy. Care must be taken to measure the DAFS spectrum far enough below and above the absorption edge up to the point where resonant scattering is negligible, otherwise the m parameter is correlated to the crystallographic phase $\varphi_T - \varphi_A$ (Proietti *et al.*, 1999).

For a rotation scan, *i.e.* with the sample rotation axis perpendicular to the plane of incidence containing \mathbf{k} and \mathbf{k}' , $L = \lambda^3/\sin 2\theta$ (Als-Nielsen & McMorrow, 2001; Prince, 2006). The polarization correction for the Thomson scattering is given by the dot product squared of the polarization vectors of the incoming and outgoing beams.

4.1. Absorption correction

The absorption correction A , which depends on the energy, is a real concern for DAFS spectroscopy. It lowers the intensity level after the edge and distorts the DAFS oscillations. For bulk, concentrated samples the effect is very strong (Vacínová *et al.*, 1995), except in grazing-incidence geometry and at subcritical incidence angles. The great advantage of nanostructured thin films is that the absorption correction is weak or negligible. In symmetric Bragg geometry, and for an incident beam projection area that is not larger than the sample surface area, the absorption of a thin film of thickness t is

$$A(\theta, E) = \frac{1}{\sin \alpha} \int_0^t \exp(-2\mu z / \sin \alpha) dz, \quad (2)$$

where α is the incidence angle and μ (m^{-1}) is the linear absorption coefficient. The prefactor $1/\sin \alpha$ takes the change

of the X-ray beam footprint into account (Prince, 2006). The absorption coefficient can be expressed as

$$\mu (\text{cm}^{-1}) = \frac{69876.576}{E (\text{eV})} [N_T f_T''(E) + N_A f_A''(E)], \quad (3)$$

where N_T and N_A are the number of nonresonant and resonant atoms per nm^3 , respectively. Equation (3) easily generalizes to the case of several different nonresonant atoms. If the film thickness is such that $2\mu(t/\sin\alpha) \ll 1$, then $A \rightarrow t/\sin\alpha$, a constant value (the incidence angle is changing very slightly in the DAFS energy range). For a bulk sample $A = 1/2\mu$. To the first order in μ , the relative absorption amplitude is $2\mu(t/\sin\alpha)$. All reflections are affected in the same way by the absorption, but weak reflections, for which resonant and nonresonant atoms scatter out of phase, are more convenient since they will exhibit larger resonant intensity variations than stronger reflections. Indeed, equation (3) in Renevier & Proietti (2022) shows that the relative resonant terms in the diffracted intensity are weighted by the ratios $|F_A|/|F_N|$ and $|F_A|/|F_N|$ squared.

In the case of an almost perfect crystal and strong reflection, Meyer *et al.* (2003) have provided a quantitative approach to correct for secondary extinction.

4.2. Crystal polarity

We have mentioned above two effects that modify the DAFS spectrum intensity level above the absorption edges, *i.e.* fluorescence (an increase) and absorption (a decrease). Only DAFS spectra corrected for the fluorescence background and absorption yield reliable $\varphi_T - \varphi_A$ values. It is worth mentioning that in the case of a noncentrosymmetric structure a difference in the diffracted intensity of Bijvoet pairs of reflections (Bijvoet *et al.*, 1951) is detected when resonant effects (f'') are significant. Friedel's law is no longer valid, *i.e.* $I(hkl) \neq I(\bar{h}\bar{k}\bar{l})$. The main effect on DAFS spectra measured with two Bijvoet pairs of reflections is the change in intensity level (an increase or decrease) after the edge because $\varphi_T - \varphi_A$ is changed to its opposite (note that this is not exactly true when taking the weak anomalous scattering of the non-resonant atoms into account). For instance, this effect is very strong in the case of the wurtzite structure (space group $P6_3mc$, polar structure) and allows the polarity of thin films and nanostructures to be determined (Hestroffer *et al.*, 2011).

4.3. Determination of the resonant scattering factors

The resonant scattering factors f_A' and f_A'' that are used to calculate the structure factors and the linear absorption μ are determined experimentally. In this way, the optical transfer function, including the monochromator resolution, the finite lifetime of the virtual excited state and the possible anisotropy of μ (in the case of a noncubic space group) are correctly taken into account. For instance, for the wurtzite structure f_A' and f_A'' strongly depend on the orientation of the beam polarization vectors with respect to the [001] polar axis. Note that, most generally, f_A' and f_A'' are tensors (Dmitrienko *et al.*, 2005). When it is relevant and possible, the imaginary part

$f_A''(E)$ is calculated from an experimental fluorescence spectrum multiplied by the beam energy and matched to a theoretical $f_A''(E)$ curve measured with the diffraction detector or a fluorescence detector close to the sample. The experimental $f_A''(E)$ curve is then Kramers–Kronig transformed to obtain $f_A'(E)$ (Cross *et al.*, 1998). Note that in the case of strong absorption, the fluorescence spectrum is distorted by self-absorption and corrections must be applied (Tröger *et al.*, 1992). Finally, calculated or tabulated values are used for nonresonant scattering factors (Chantler, 1995).

5. Extended DAFS analysis

Together with technical improvements, data analysis has also improved, relying on one hand on the solid support of the established MAD data treatment and on the other hand on the EXAFS approach (Stragier *et al.*, 1992) with available and well-known codes for *ab initio* calculations, data simulation and analysis. A DAFS spectrum contains contributions from both the real and imaginary parts of the complex resonant scattering factors, whereas XAFS is only proportional to the imaginary part. In the simplest case, where the resonant atoms are located on one crystallographic site only, one can use equation (3) in Renevier & Proietti (2022) to perform an iterative Kramers–Kronig analysis and recover $f_A'(E)$ and $f_A''(E)$ (Cross *et al.*, 1998). In the case of a noncentrosymmetric structure with several resonant crystallographic sites, the iterative Kramers–Kronig procedure cannot be applied due to the presence of $f'f''$ cross terms. Alternatively, the extended-region DAFS (EDAFS) above the edge can be analyzed according to a first-order approximation in χ_Q (see Section 3.1 of Renevier & Proietti, 2022), such as EXAFS oscillations (Proietti *et al.*, 1999). Basically, the analysis consists of the following.

(i) Fitting equation (1) to the DAFS spectrum cusp (corrected for fluorescence) gives the scale factor S_D (see equation 7 in Renevier & Proietti, 2022) and the crystallographic phase $\varphi_0 - \varphi_A$ (see equation 8 in Renevier & Proietti, 2022).

(ii) χ_Q is obtained by multiplying S_D by $[(I - I_0)/I_0](Q, E)$ (where I_0 is the smooth diffracted intensity, *i.e.* without oscillations). The phase difference $\varphi_0 - \varphi_A$ is added to the XAFS theoretical phase provided, for example, by the *FEFF* code (Ankudinov *et al.*, 2002; Kas *et al.*, 2020).

(iii) The new theoretical XAFS phases are used to analyze χ_Q , for instance with the *IFEFFIT* code (Newville, 2001; Newville & Ravel, 2020) implemented in the *ARTEMIS* package (Ravel & Newville, 2005, 2020).

Note that the path-by-path multiple-scattering approach is no longer valid in the energy region close to the absorption edge (Rehr & Albers, 2000). However, as in the case of X-ray absorption near-edge structure (XANES), the anomalous diffraction near-edge structure (DANES) can be calculated with a dedicated program, such as for instance *FDMNES* (see Joly, 2001; Bunău *et al.*, 2021).

6. Conclusion

In this chapter we give a brief state-of-the-art survey of the DAFS technique, describing its most important experimental and data-reduction aspects. We provide a basic bibliography to approach the use of DAFS. DAFS combines the capabilities of X-ray absorption and diffraction techniques and is particularly suited to the study of the structural properties of low-dimensionality systems such as thin films and nanostructures.

References

- Als-Nielsen, J. & McMorrow, D. (2001). *Elements of Modern X-ray Physics*, 1st ed. New York: John Wiley & Sons.
- Ankudinov, A., Bouldin, C., Rehr, J., Sims, J. & Hung, H. (2002). *Phys. Rev. B*, **65**, 104107.
- Bijvoet, J. M., Peerdeman, A. F. & van Bommel, A. J. (1951). *Nature*, **168**, 271–272.
- Bunău, O., Ramos, A. Y. & Joly, Y. (2021). *Int. Tables Crystallogr. I*, <https://doi.org/10.1107/S1574870720003304>.
- Chantler, C. T. (1995). *J. Phys. Chem. Ref. Data*, **24**, 71–643.
- Coraux, J., Favre-Nicolin, V., Proietti, M. G., Daudin, B. & Renevier, H. (2007). *Phys. Rev. B*, **75**, 235312.
- Cross, J., Newville, M., Rehr, J., Sorensen, L., Bouldin, C., Watson, G., Gouder, T., Lander, G. & Bell, M. (1998). *Phys. Rev. B*, **58**, 11215–11225.
- Dmitrienko, V. E., Ishida, K., Kirfel, A. & Ovchinnikova, E. N. (2005). *Acta Cryst.* **A61**, 481–493.
- Favre-Nicolin, V., Proietti, M. G., Leclerc, C., Katcho, N. A., Richard, M. I. & Renevier, H. (2012). *Eur. Phys. J. Spec. Top.* **208**, 189–216.
- Hestroffer, K., Leclerc, C., Bougerol, C., Renevier, H. & Daudin, B. (2011). *Phys. Rev. B*, **84**, 245302.
- Hodeau, J., Favre-Nicolin, V., Bos, S., Renevier, H., Lorenzo, E. & Berar, J. (2001). *Chem. Rev.* **101**, 1843–1867.
- Joly, Y. (2001). *Phys. Rev. B*, **63**, 125120.
- Kas, J. J., Vila, F. D. & Rehr, J. J. (2020). *Int. Tables Crystallogr. I*, <https://doi.org/10.1107/S1574870720003274>.
- Katcho, N. A., Richard, M., Proietti, M. G., Renevier, H., Leclerc, C., Favre-Nicolin, V., Zhang, J. J. & Bauer, G. (2011). *EPL*, **93**, 66004.
- Kegel, I., Metzger, T. H., Lorke, A., Peisl, J., Stangl, J., Bauer, G., Nordlund, K., Schoenfeld, W. V. & Petroff, P. M. (2001). *Phys. Rev. B*, **63**, 035318.
- Meyer, D. C., Kupsch, A. & Paufler, P. (2003). *J. Synchrotron Rad.* **10**, 144–147.
- Newville, M. (2001). *J. Synchrotron Rad.* **8**, 322–324.
- Newville, M. & Ravel, B. (2020). *Int. Tables Crystallogr. I*, <https://doi.org/10.1107/S1574870720003407>.
- Prince, E. (2006). *International Tables for Crystallography*, Vol. C, 1st online ed. Chester: International Union of Crystallography.
- Proietti, M., Renevier, H., Hodeau, J., García, J., Béar, J. & Wolfers, P. (1999). *Phys. Rev. B*, **59**, 5479–5492.
- Ravel, B. & Newville, M. (2005). *J. Synchrotron Rad.* **12**, 537–541.
- Ravel, B. & Newville, M. (2020). *Int. Tables Crystallogr. I*, <https://doi.org/10.1107/S1574870720003353>.
- Rehr, J. J. & Albers, R. C. (2000). *Rev. Mod. Phys.* **72**, 621–654.
- Renevier, H., Grenier, S., Arnaud, S., Béar, J. F., Caillot, B., Hodeau, J. L., Letoublon, A., Proietti, M. G. & Ravel, B. (2003). *J. Synchrotron Rad.* **10**, 435–444.
- Renevier, H., Hodeau, J., Wolfers, P., Andrieu, S., Weigelt, J. & Frahm, R. (1997). *Phys. Rev. Lett.* **78**, 2775–2778.
- Renevier, H. & Proietti, M. G. (2013). *Characterization of Semiconductor Heterostructures and Nanostructures*, 2nd ed., edited by C. Lamberti & G. Agostini, pp. 311–359. Amsterdam: Elsevier.
- Renevier, H. & Proietti, M. G. (2022). *Int. Tables Crystallogr. I*, <https://doi.org/10.1107/S1574870720007570>.
- Sorensen, L., Cross, J., Newville, M., Ravel, B., Rehr, J. J., Stragier, H., Bouldin, C. & Woicik, J. (1994). In *Resonant Anomalous X-ray Scattering: Theory and Applications*, edited by G. Materlik, J. Sparks & K. Fischer. Amsterdam: Elsevier.
- Stragier, H., Cross, J., Rehr, J., Sorensen, L., Bouldin, C. & Woicik, J. (1992). *Phys. Rev. Lett.* **69**, 3064–3067.
- Tröger, L., Arvanitis, D., Baberschke, K., Michaelis, H., Grimm, U. & Zschech, E. (1992). *Phys. Rev. B*, **46**, 3283–3289.
- Vacínová, J., Hodeau, J. L., Wolfers, P., Lauriat, J. P. & ElKaim, E. (1995). *J. Synchrotron Rad.* **2**, 236–244.